

Imaging observations of chromospheric evaporation in a circular-ribbon flare

Q. M. ZHANG,¹ D. LI,^{1,2,3} AND Y. HUANG¹

¹Key Laboratory for Dark Matter and Space Science, Purple Mountain Observatory, CAS, Nanjing 210034, China

²State Key Laboratory of Space Weather, Chinese Academy of Sciences, Beijing 100190, PR China

³CAS Key Laboratory of Solar Activity, National Astronomical Observatories, Beijing 100012, China

(Received November 1, 2018; Revised November 1, 2018; Accepted November 29, 2018)

Submitted to ApJ

ABSTRACT

In this paper, we report our multiwavelength imaging observations of chromospheric evaporation in a C5.5 circular-ribbon flare (CRF) on 2014 August 24. The flare was observed by the Atmospheric Imaging Assembly (AIA) on board the *Solar Dynamics Observatory* (SDO), X-ray Telescope (XRT) on board the *Hinode* spacecraft, and ground-based Nobeyama Radioheliograph (NoRH). The CRF consisted of a discrete circular ribbon with a diameter of $\sim 1'$ and a short inner ribbon observed in ultraviolet (UV), extreme-ultraviolet (EUV), soft X-ray (SXR), and especially in 17 GHz. The peak time ($\sim 04:58$ UT) of the flare in 17 GHz coincided with that in UV 1600 Å and SXR derivative as a hard X-ray proxy, implying the peak time of impulsive energy deposition in the lower atmosphere. Shortly after the peak time, converging motion and filling process in the flare loop were revealed in AIA 131 Å and two XRT filters (Be_{thin} and Be_{med}), which are clear evidence for chromospheric evaporation upflows. The chromospheric evaporation lasted for ~ 6 minutes until $\sim 05:04$ UT. The temperature, density, and apparent velocities of the upflows are $\sim 10^7$ K, $\sim 1.8 \times 10^{10}$ cm⁻³, and 50–630 km s⁻¹ with a mean value of ~ 170 km s⁻¹. By comparison with previous models, we are able to estimate that energies above 5×10^{10} erg cm⁻² s⁻¹ are likely needed to explain the observational results. Since heating by thermal conduction does not seem to provide enough energy, alternative mechanisms such as nonthermal electrons or Alfvénic waves might need to be invoked.

Keywords: Sun: chromosphere — Sun: flares — Sun: UV radiation — Sun: X-rays, gamma rays

1. INTRODUCTION

Solar flares are impulsive increases of electromagnetic emissions from radio wave to γ -ray as a result of the release of magnetic free energy of 10^{29} – 10^{32} erg (Fletcher et al. 2011; Shibata & Magara 2011; Warmuth & Mann 2016a,b). The accumulated magnetic energy

is converted to the kinetic and thermal energy of the reconnection outflows as well as the nonthermal energy of accelerated particles via magnetic reconnection (e.g., Holman et al. 2011; Tian et al. 2014; Yang et al. 2015). In the two-dimensional (2D) standard flare model, the high-energy electrons propagate downward along the reconnected magnetic field and precipitate in the chromosphere (Carmichael 1964; Sturrock 1966; Hirayama 1974; Kopp & Pneuman 1976). The collision of electrons with ions result in impulsive heating of the localized plasma and increases of radiations in hard X-ray (HXR) and microwave (Brown 1971; Bastian et al. 1998). If the heating rate in the chromosphere is significantly larger than the energy dissipation rate, the hot plasmas would flow upward along the flare loops driven by overpressure, a process called chromospheric evaporation (Acton et al. 1982; Fisher et al. 1985a,b,c; Canfield et al. 1990; Abbett & Hawley 1999; Allred et al. 2005). Meanwhile, the dense plasmas experience downward motion at much smaller speeds due to the momentum balance, a process called chromospheric condensation (Fisher 1989; Wuelser et al. 1994). There are two types of chromospheric evaporation. For the explosive evaporation, the emission lines formed in the corona are blueshifted, while the emission lines formed in the transition region and chromosphere are redshifted (e.g., Czaykowska et al. 1999; Brosius & Phillips 2004; Milligan & Dennis 2009; Brosius 2013; Li et al. 2015). The velocities of the blueshifted upflows are 100–800 km s⁻¹, while the velocities of the redshifted downflows are tens of km s⁻¹. For the gentle evaporation, the lines can show blue- or no shift (e.g., Milligan et al. 2006; Battaglia et al. 2009; Sadykov et al. 2015). Based on the assumption that the electron beams last for 5 s, with a fixed energy flux, a fixed spectral index ($\delta = 4$), and a fixed low-energy cut-off ($E_c = 20$ keV), Fisher et al. (1985c) derived the

threshold for the input energy flux of explosive evaporation ($\sim 10^{10}$ erg cm⁻² s⁻¹). However, it is recently found that the threshold (F) depends strongly on the electron energy (E_*) and duration of heating (Reep et al. 2015). The relationship between F and E_* is linearly fitted in log-log space, $\log_{10} F = 6.99 + 2.43 \log_{10} E_*$ (see their Fig. 7). Chromospheric evaporations mainly take place in the impulsive and decay phases of flares. However, they occasionally occur in the pre-flare phase (Brosius & Holman 2010; Li et al. 2018). For the driving mechanisms of chromospheric evaporation, the role of nonthermal electrons has been richly investigated and widely accepted (Reep et al. 2015; Rubio da Costa et al. 2015). In some cases, thermal conduction plays an essential role (Falchi et al. 1997; Battaglia et al. 2009).

There are abundant observations of chromospheric evaporation in solar flares, most of which are spectroscopic (e.g., Young et al. 2013, 2015; Polito et al. 2015, 2016; Milligan 2015; Tian & Chen 2018). So far, direct imaging observations of chromospheric evaporation are rare owing to the limited spatial and temporal resolutions of solar telescopes. One way of detecting the evaporation upflow is the rapid lifting and converging motions of double sources along the flare loops in HXR and microwave wavelengths (Aschwanden et al. 1995; Liu et al. 2006; Ning et al. 2009; Ning & Cao 2010). The other way is direct imaging of the upflow in extreme-ultraviolet (EUV) and SXR wavelengths (e.g., Silva et al. 1997; Nitta et al. 2012; Zhang & Ji 2013; Li et al. 2017a).

Circular-ribbon flares (CRFs) are observed and investigated in detail by Masson et al. (2009). As its name implies, the ribbons of CRFs have circular or quasi-circular shapes in Ca II H, H α , UV, and EUV wavelengths (Sun et al. 2012; Wang & Liu 2012; Jiang et al. 2013; Kumar et al. 2016; Hao et al. 2017; Li et al. 2017b; Song et al. 2018). The magnetic topol-

ogy of CRFs are mostly associated with a magnetic null point ($\mathbf{B} = 0$), a spine, and a dome-like fan surface (Zhang et al. 2012, 2015). Zhang et al. (2016a) studied a C4.2 CRF on 2015 October 16 observed by the *Interface Region Imaging Spectrograph* (IRIS; De Pontieu et al. 2014). For the first time, the authors found explosive chromospheric evaporation in the circular ribbon (CR) and inner ribbon (IR). Upflows at a speed of 35–120 km s⁻¹ are observed in the high-temperature Fe XXII $\lambda 1354.09$ line ($\log T \approx 7.05$), and downflows at a speed of 10–60 km s⁻¹ are observed in the low-temperature Si IV $\lambda 1393.77$ line ($\log T \approx 4.8$). In a follow-up work, Zhang et al. (2016b) reported periodic chromospheric condensation in a homologous CRF in the same active region (AR). However, direct imaging observation of chromospheric evaporation in CRFs has never been investigated. In this paper, we report our multiwavelength observations of chromospheric evaporation in a C5.5 CRF on 2014 August 24. In Section 2, we describe the observations and data analysis. Results are present in Section 3. We compare our findings with previous works in Section 4 and give a brief summary in Section 5.

2. DATA ANALYSIS

The C5.5 flare took place in NOAA AR 12149 (N10E44). It was observed by the Atmospheric Imaging Assembly (AIA; Lemen et al. 2012) on board the *Solar Dynamics Observatory* (SDO) spacecraft. AIA takes full-disk images in two UV (1600 and 1700 Å) and seven EUV (94, 131, 171, 193, 211, 304, and 335 Å) wavelengths. The photospheric line-of-sight (LOS) magnetograms were observed by the Helioseismic and Magnetic Imager (HMI; Scherrer et al. 2012) on board SDO. The AIA and HMI level_1 data were calibrated using the standard *Solar Software* (SSW) program *aia_prep.pro* and *hmi_prep.pro*, respectively. The flare was also captured by the X-ray Telescope (XRT; Golub et al. 2007) on board the *Hinode* (Kosugi et al. 2007) space-

Table 1. Description of the observational parameters

Instru.	λ (Å)	Time (UT)	Cad. (s)	Pix. size ($''$)
<i>SDO/AIA</i>	94–335	04:30–06:00	12	0.6
<i>SDO/AIA</i>	1600	04:30–06:00	24	0.6
<i>SDO/HMI</i>	6173	04:30–06:00	45	0.6
<i>Hinode/XRT</i>	Be_thin	04:33–05:41	~30	1.03
<i>Hinode/XRT</i>	Be_med	04:58–05:08	~20	1.03
<i>GOES</i>	0.5–4	04:30–06:00	2.05	...
<i>GOES</i>	1–8	04:30–06:00	2.05	...
NoRH	17 GHz	04:30–06:00	1	5

craft with a smaller field of view ($384'' \times 384''$). The SXR images observed by the Be_thin and Be_med filters were calibrated using the standard SSW program *xrt_prep.pro* and coaligned with the AIA 131 Å images. SXR fluxes of the flare in 0.5–4 Å and 1–8 Å were recorded by the *GOES* spacecraft. The Nobeyama Radioheliograph (NoRH; Nakajima et al. 1994) at the Nobeyama Radio Observatory also observed this flare. As a ground-based radio telescope, NoRH observes the full disk at frequencies of 17 and 34 GHz with spatial resolutions of 10 $''$ and 5 $''$, respectively. The observational parameters, including the instrument, wavelength, time cadence, and pixel size are summarized in Table 1.

In order to have a better evaluation of the temperature and density of the flare, we performed differential emission measure (DEM) analysis using the simultaneous AIA images in six EUV wavelengths (94, 131, 171, 193, 211, 335 Å). The EUV flux of the optically thin plasma at a certain passband is expressed as

$$F_i = \int_{T_1}^{T_2} R_i(T) \times \text{DEM}(T) dT, \quad (1)$$

where $R_i(T)$ is the temperature response function of passband i , T_1 and T_2 represent the minimum and maximum temperatures, and

DEM(T) stands for DEM as a function of T (Zhang & Ji 2014; Zhang et al. 2016c). The total column emission measure (EM) along the LOS depth (H) is defined as the integral of DEM(T),

$$\text{EM} = \int_{T_1}^{T_2} \text{DEM}(T) dT \approx n_e^2 H, \quad (2)$$

where n_e denotes the electron number density. The DEM-weighted average temperature (\bar{T}) is expressed as

$$\bar{T} = \frac{\int_{T_1}^{T_2} \text{DEM}(T) \times T dT}{\text{EM}}. \quad (3)$$

To improve the signal to noise ratio, we performed a 2×2 binning of the images. A small patch of quiet region outside the flare region is taken as the background, whose intensities are removed before conducting the DEM analysis. Besides, we take $\log T_1 = 5.5$ and $\log T_2 = 7.5$ in the inversion. The method and code are the same as those we previously used (Zhang & Ji 2014; Zhang et al. 2016c).

3. RESULTS

3.1. Circular-ribbon flare and jets

In Figure 1(a), the SXR light curves of the flare in $0.5\text{--}4 \text{ \AA}$ and $1\text{--}8 \text{ \AA}$ are plotted with magenta and cyan lines, respectively. The fluxes increase slowly during the pre-flare phase (04:50–04:55 UT). Afterwards, the fluxes increase rapidly during the impulsive phase (04:55–05:02 UT). Then, the emissions decline gradually until $\sim 05:25$ UT. Hence, the lifetime of the flare is about 0.5 hr. Considering that HXR observation of the flare during the impulsive phase is unavailable, we take the time derivative of the light curve in $1\text{--}8 \text{ \AA}$ as a HXR proxy based on the Neupert effect (Neupert 1968), which is plotted in Figure 1(b). Two peaks at 04:58 UT and 04:59 UT are noticeable. The duration of chromospheric heating by nonthermal electrons is defined as the full

width at half maximum (FWHM) of the HXR light curve, which is indicated by the orange horizontal arrow. In order to derive the light curve in 17 GHz, we integrate the intensities of the whole flare region (see Figure 3(b)). The light curve is plotted in Figure 1(c). Two sharp spikes at 04:56:27 UT and 04:57:58 UT superposed on the gradual component are identified. The second spike coincides with the first peak in HXR proxy indicated by the black dashed line. The spikes in microwave are in fact clear evidence of gyrosynchrotron emission by non-thermal electrons. Likewise, we derived the UV light curve by integrating the intensities of the flare region in 1600 \AA (see Figure 3(a)). The normalized curve is plotted in Figure 1(d). The same peak shows up at 04:58 UT, although the time cadence is relatively lower. The weaker peak around 04:59 UT is coincident with that in HXR proxy. Combining the light curves in multiwavelengths, we conclude that the peak of the energy deposition in the lower atmosphere carried by nonthermal electrons took place around 04:58 UT.

In Figure 2, the whole evolution of the flare is represented by eight snapshots in 171 \AA . In the pre-flare phase, AR 12149 was somewhat quiet (see panel (a)). Four minutes later, the first jet (jet1) appeared and propagated in the northeast direction along a closed coronal loop (see panel (b)). At $\sim 04:58$ UT, the intensities of the discrete CR and IR of the CRF reached their maxima (see panel (c)). Soon after, a second jet (jet2) spurted out of the flare in the north direction before deflecting eastward (see panels (d)-(e)). The intensities of flare loops and jets decreased gradually and faded out (see panel (h)).

In Figure 3(c), the HMI LOS magnetogram at 04:58:23 UT is displayed in grayscale. The white arrow points to AR 12149 with mixed polarities. A closeup of the flare region with a field of view (FOV) of $80'' \times 80''$ is demonstrated in

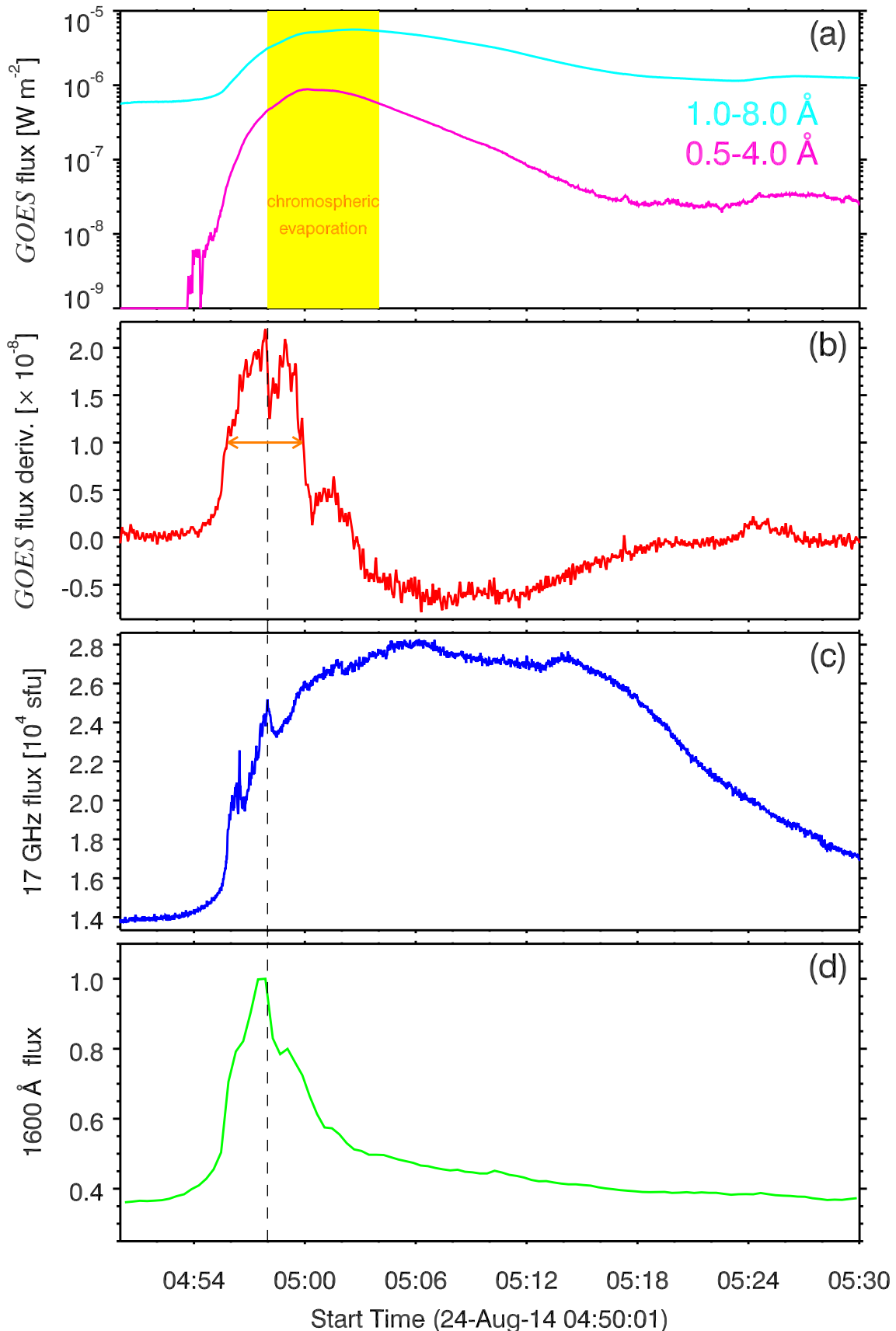


Figure 1. (a)-(d) Light curves of the C5.5 flare in SXR, HXR proxy (time derivative of the light curve in 1–8 Å), 17 GHz, and 1600 Å (normalized). The black dashed line denotes the time at 04:57:58 UT. In panel (a), the yellow region stands for the time of chromospheric evaporation. In panel (b), the orange horizontal arrow denotes the duration of heating by nonthermal electrons (~ 4 minutes).

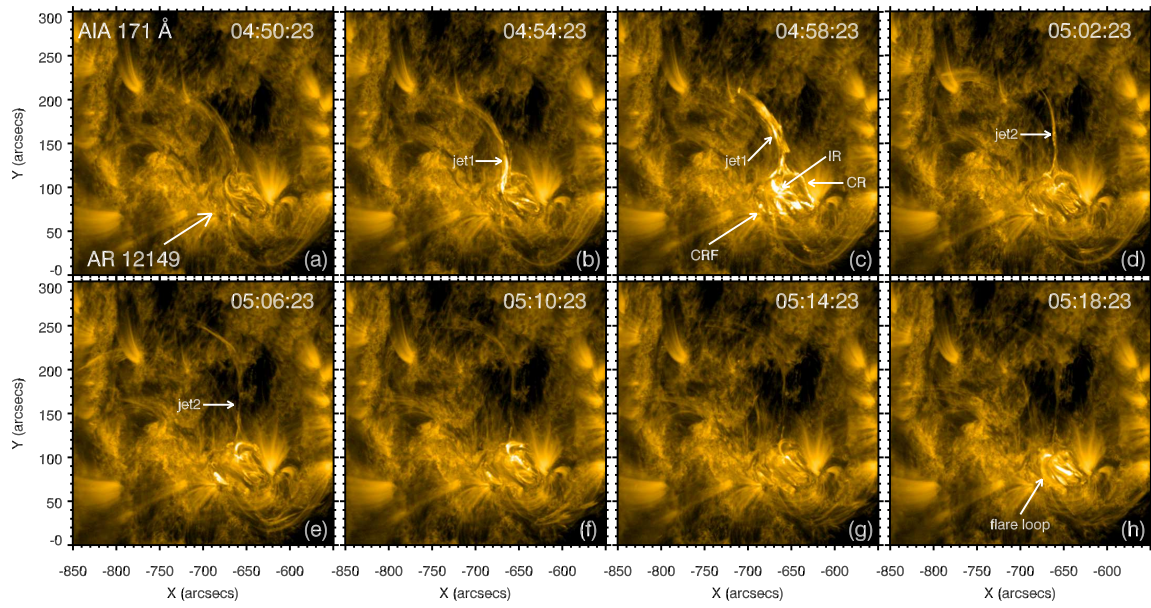


Figure 2. Eight snapshots of the AIA 171 Å images during 04:50–05:18 UT. The white arrows point to AR 12149, CRF, CR, IR, jet1, and jet2.

panel (d). The most conspicuous feature of the magnetogram is that positive polarities are surrounded by negative polarities. The AIA 1600 Å image and NoRH 17 GHz image around 04:58 UT with the same small FOV are displayed in the top panels. We superpose the intensity contours of the UV image on panel (d) with cyan lines. It is obvious that the IR is cospatial with the positive polarities and the discrete CR is cospatial with negative polarities, which is similar to the case of C-class CRFs on 2015 October 16 (Zhang et al. 2016a,b). Such a correspondence between the flare ribbons and magnetic polarities is strongly suggestive of the existence of a magnetic null point and the fan-spine configuration in the corona. The radio image, although with a lower resolution, features three bright patches (BPs) pointed by the white arrows. Likewise, we superpose the intensity contours of radio image on panel (a) with orange lines. The most prominent patch (BP1) is cospatial with the IR and the weaker surrounding patches (BP2 and BP3) are cospatial with the CR. To our knowledge, this is the first detection of distinguishable ribbons of CRFs in microwave.

In Figure 4, the left panels show images taken by the XRT filters around 04:58 UT. The SXR emissions of the flare come from the hot plasmas of several MK and have similar morphology to the EUV images (see Figure 2(c)). The large-scale coronal loop above the flare is the loop that guides jet1.

3.2. Chromospheric evaporation

In Figure 5, nine snapshots of AIA 131 Å images illustrate the converging motion along the hot flare loop. Shortly after the peak times (\sim 04:58 UT) in UV and radio wavelengths, the flare loops are empty (see panel (a)). As time goes on, hot plasmas move from the double footpoints (FP1 and FP2) towards the loop top (see panels (c)-(e)). The intensities of the loops gradually increase during the upward converg-

ing motion and filling process (see panels (g)-(i)). In panel (e), the contours of the positive and negative magnetic polarities at 05:02:08 UT are superposed with blue and yellow lines. FP2 and FP1 are rooted in positive and negative polarities, which are associated with the IR and CR (see Figure 3(d)).

To investigate the temporal evolution of the flare loop, we derive the intensities along the curved slice (S0) with a length of 50'' in Figure 5(a). The time-slice diagrams of S0 in six EUV wavelengths are displayed in Figure 6. In panel (a), the converging motion from the footpoints towards the loop top during 04:58–05:04 UT is clearly demonstrated. The intensities of flare loops filled with hot plasmas reach their maxima around 05:06 UT. Such converging motion and filling process within the flare loops are strongly indicative of chromospheric evaporation in the CRF, which can not be identified in the cooler lines.

After carefully examining the SXR images observed by *Hinode*/XRT, we found similar filling process of the flare loops. In Figure 7, the time-slice diagrams of S0 in 94 Å and 131 Å are displayed in the left panels, and the diagrams in SXR are displayed in the right panels. It is obvious that the converging motion in 131 Å outlined by the black dashed line is coincident with that in SXR. In panel (a), there seems to be converging motion in 94 Å. However, we are not quite sure of that since it is very blurring.

The apparent velocities of the converging flow are represented by the slopes (ds/dt) of the dashed line in Figure 7(c). For a certain position s_i , the velocity is expressed as $v_i = (s_{i+1} - s_{i-1}) / (t_{i+1} - t_{i-1})$. The uncertainties of velocity come from the uncertainties of time. In Figure 8, the spatial distribution of the apparent velocities along the flare loop is plotted with red circles. It is seen that the velocities range from 50 to 630 km s⁻¹, with a mean value of \sim 170 km

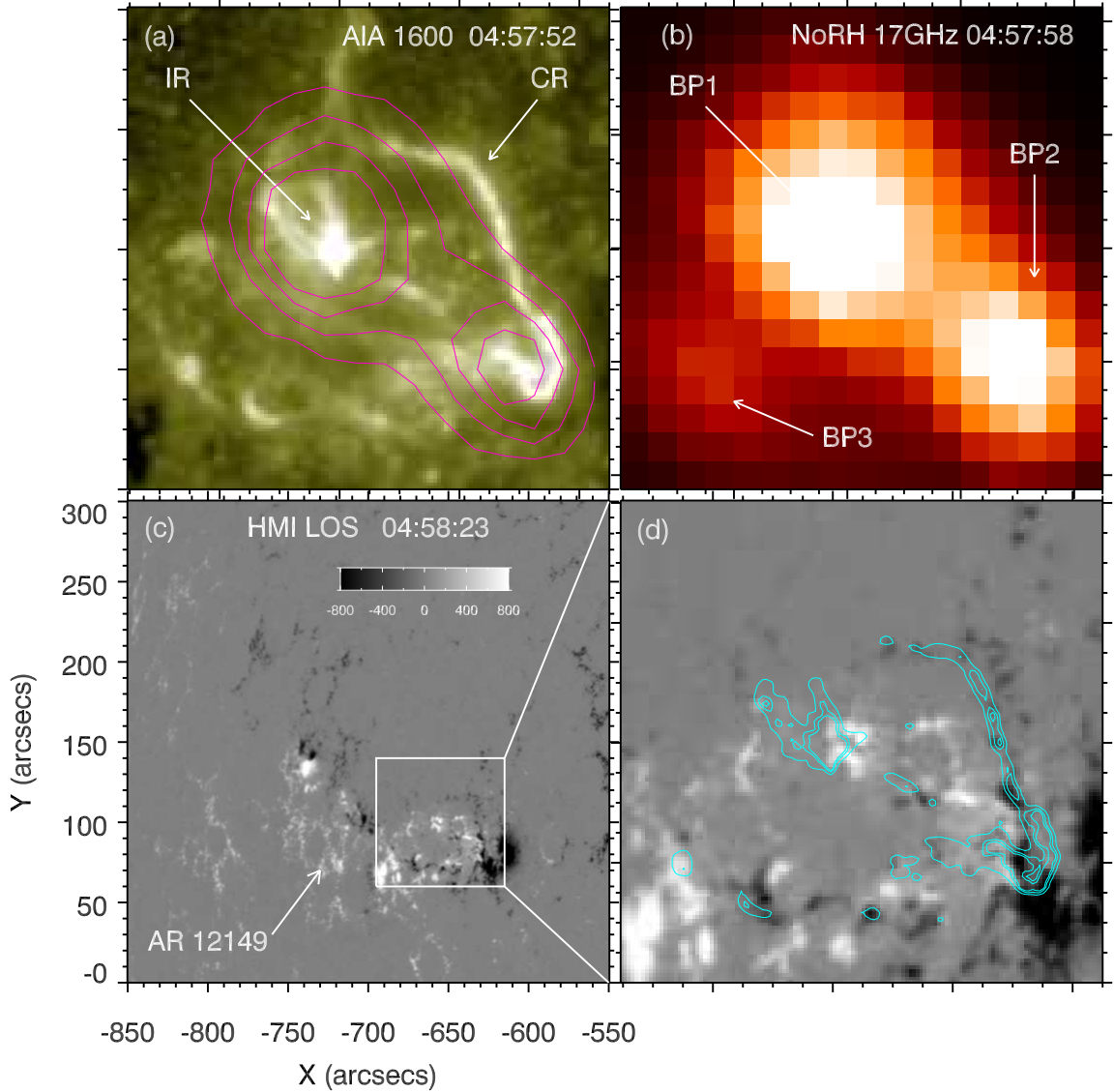


Figure 3. *Bottom panels:* HMI LOS magnetogram at 04:58:23 UT and a closeup of the flaring region. White and black colors represent positive and negative polarities. *Top panels:* AIA 1600 Å image and NoRH 17 GHz image around 04:58 UT with the same FOV as panel (d). Intensity contours (50%, 70%, 90%) of the radio image are superposed on panel (a) with orange lines. Intensity contours of the 1600 Å image are superposed on panel (d) with cyan lines.

s^{-1} . The error bars of velocity increase sharply from the footpoints to the loop apex.

Figure 9 shows the emission measure map and temperature map of the flare before the completeness of chromospheric evaporation. The flare region with high density and temperature is well reproduced, which is in accordance with the EUV and SXR observations (see Figure 4). The right panel indicates that the temperatures

of flare loops can reach ~ 10 MK, which is in agreement with our evaluation from Figure 6. It should be emphasized that the flare loop is not a single flux tube, but consist of a bundle of ultra-fine strands in deed (Jing et al. 2016). However, the strands could not be precisely distinguished in 131 Å. In Figure 5(f), we measured the apparent width of the flare loop, which is about $8''$. The LOS depth (H) equals to the width as-

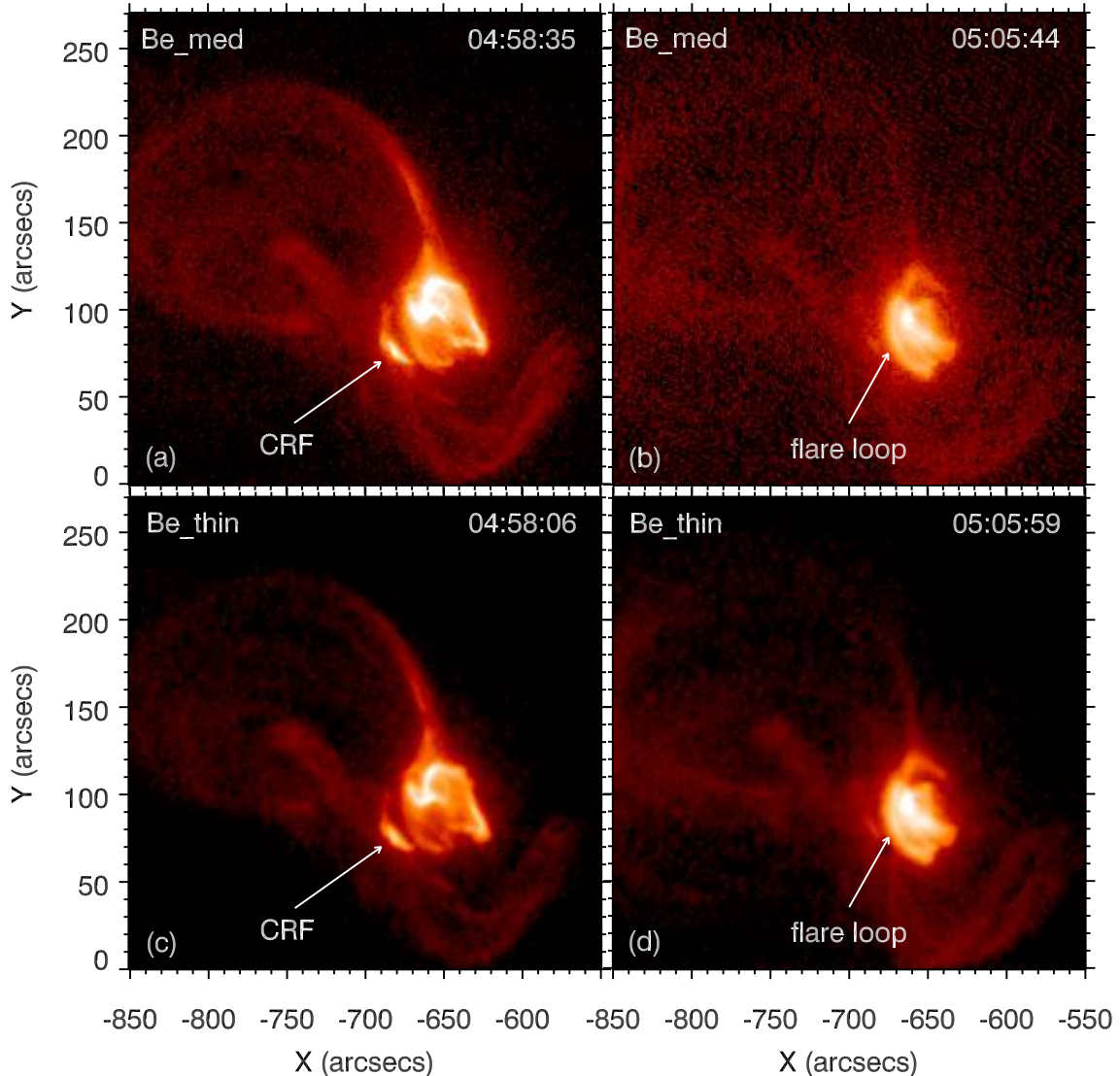


Figure 4. SXR images taken by XRT/Be_med and XRT/Be_thin filters around 04:58 UT (*left panels*) and 05:06 UT (*right panels*). The white arrows point to the CRF and flare loop.

suming a cylindric flux tube. Taking the value of EM near the loop top ($\sim 1.9 \times 10^{29} \text{ cm}^{-5}$), the electron number density (n_e) is estimated to be $\sim 1.8 \times 10^{10} \text{ cm}^{-3}$ according to Equation 2.

Figure 6 shows that the flare loop became prominent progressively from $\sim 05:06$ UT in 131 Å to $\sim 05:20$ in 171 Å, which is a clear indication of cooling process. Considering that thermal conductive cooling dominates over radiative cooling for hot plasmas (~ 10 MK), the cooling

timescale is expressed as

$$\tau_c = 4 \times 10^{-10} \frac{n_e L^2}{T_e^{5/2}}, \quad (4)$$

where n_e , T_e , and L represent the electron number density, temperature, and total length of a coronal loop (Cargill 1994). According to the estimated values of $n_e = 1.8 \times 10^{10} \text{ cm}^{-3}$, $T_e = 10^7 \text{ K}$, and $L = 5.7 \times 10^9 \text{ cm}$ with a semi-circular shape, τ_c is estimated to be 12 minutes, which is roughly consistent with the cooling time (14 minutes) of the flare loop.

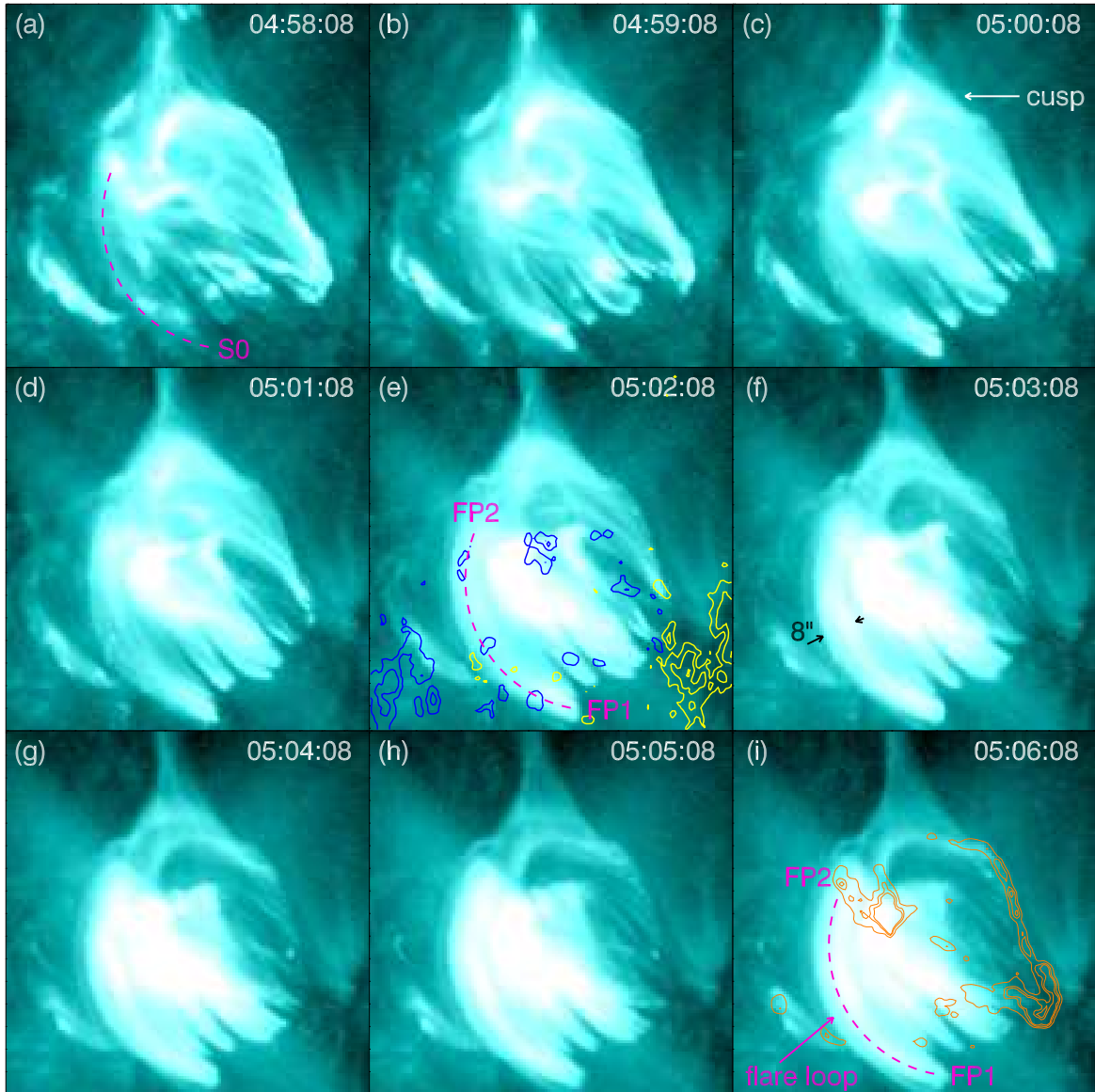


Figure 5. AIA 131 Å images during the chromospheric evaporation. In panels (a), (e), and (i), the short slice (S0) along the hot flare loop is labeled with a magenta dashed line. “FP1” and “FP2” signify the south and north footpoints of the flare loop. The blue and yellow lines in panel (e) represent the positive and negative polarities. Intensity contours of the 1600 Å image at 04:57:52 UT are superposed on panel (i) with brown lines.

4. DISCUSSION

Chromospheric evaporation has been extensively studied in the past three decades. The temperatures of evaporation upflows can reach tens of millions degrees (e.g., Young et al. 2013; Tian et al. 2014; Li et al. 2015; Polito et al. 2015; Zhang et al. 2016a). In this study, the converging motion from the footpoints to the loop top and filling process in the flare loop

are simultaneously observed by *SDO/AIA* in 131 Å and the SXR filters on board XRT. The hot evaporation upflow is further justified by the DEM analysis. During the impulsive phase of C4.2 CRF on 2015 October 16, upflows at speeds of 35–120 km s⁻¹ on the flare ribbons are detected in the Fe XXI λ 1354.09 emission line ($\log T \approx 7.05$) (Zhang et al. 2016a). Hence, the spectroscopic and imaging observations consol-

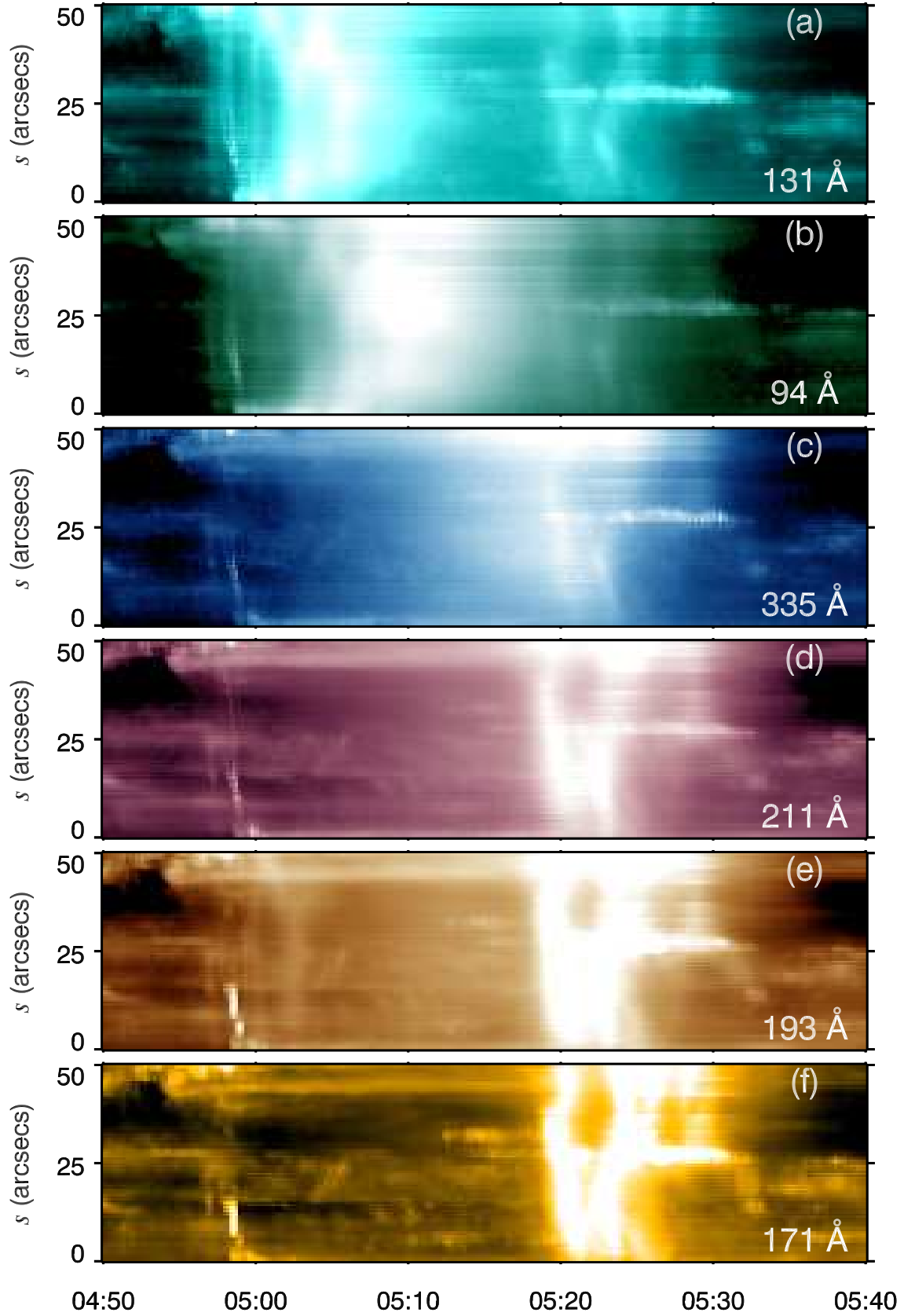


Figure 6. Time-slice diagrams of S0 in six EUV wavelengths. $s = 0$ and $s = 50''$ in the y -axis denote FP1 and FP2, respectively. Note that the intensities are in logarithmic scale.

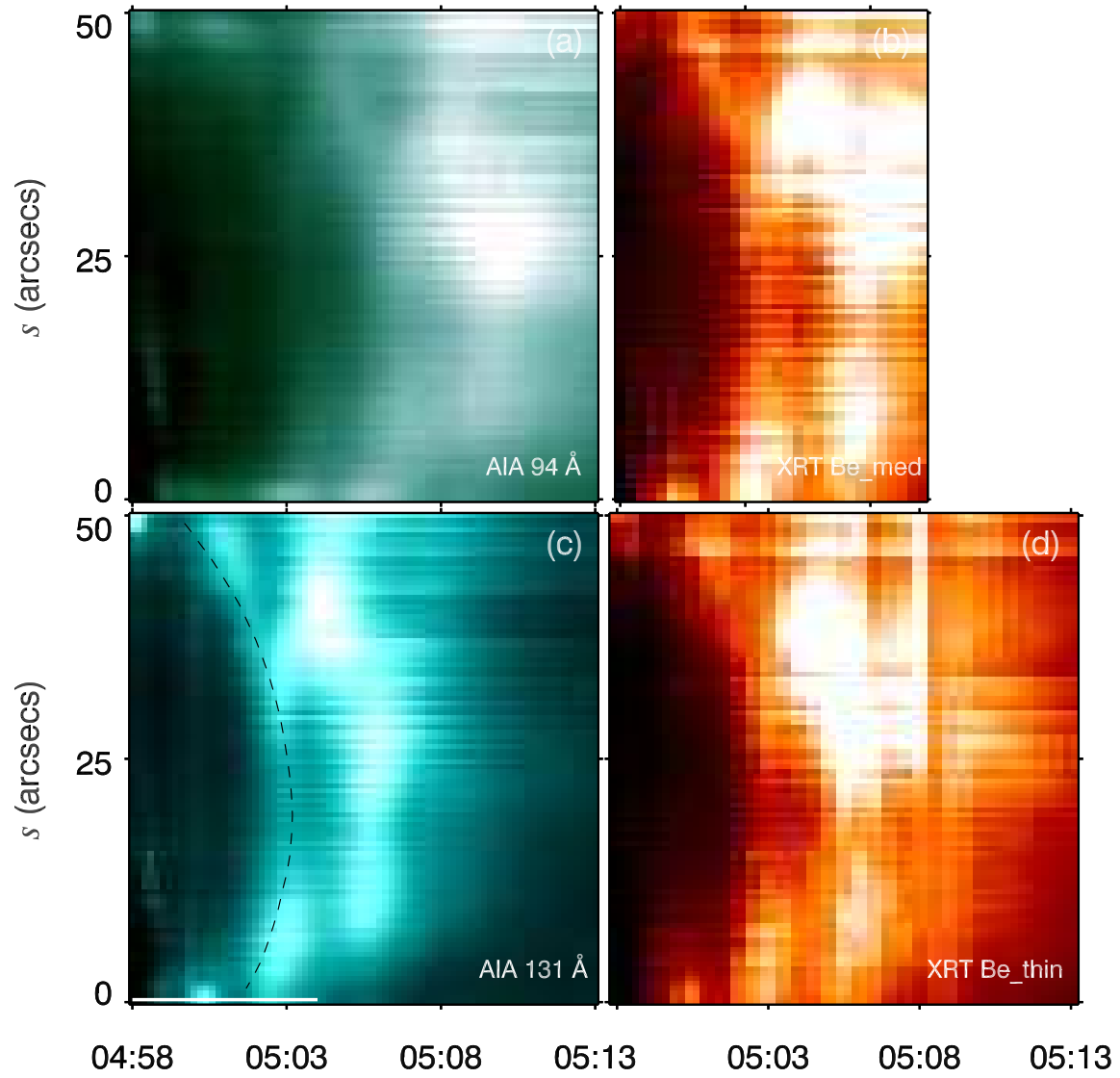


Figure 7. Time-slice diagrams of S0 in AIA 94 Å (a), 131 Å (c), XRT Be_med (b), and Be_thin (d) filters. In panel (c), the converging motion is outlined by a black dashed line. The horizontal line signifies the duration of evaporation from 04:58 UT to 05:04 UT. Note that the intensities are in linear scale.

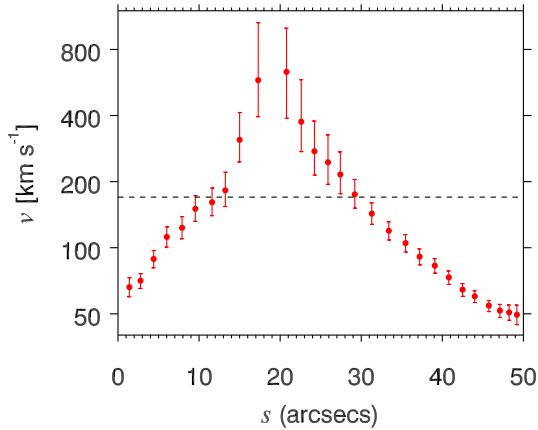


Figure 8. Spatial distribution of the apparent velocities of the converging flow along the flare loop. The mean value ($\sim 170 \text{ km s}^{-1}$) is denoted by the black dashed line.

idate the existence of high-temperature evaporation upflows in CRFs. Using the apparent width of the flare loop, we also estimated the electron number density of the evaporation upflow. The value ($1.8 \times 10^{10} \text{ cm}^{-3}$) is 1–2 orders of magnitude lower than that in the flare loops on 2014 October 27 (Polito et al. 2016). One plausible reason is that the estimated value is a lower limit assuming that the filling factor of plasma equals to 1.0.

In previous studies of direct imaging observations of chromospheric evaporation in EUV and SXR wavelengths, the velocities of upflows range from 100 to 500 km s^{-1} (Silva et al. 1997; Nitta et al. 2012; Li et al. 2017a). Another way of detecting the chromospheric evaporation is to track the HXR footpoint sources along the flare loops. The velocities of drifting or converging motions of the sources are reported to be a few hundred km s^{-1} (Liu et al. 2006; Ning et al. 2009; Ning & Cao 2010). In this study, the flare loops are observed head-on rather than edge-on. Therefore, the measured velocities (50–630 km s^{-1}) of the evaporation upflows are projected or apparent velocities. The true values, after correcting the projection effect with the assumption of a semicircular shape, should be larger by a factor of ~ 1.5 near the footpoints. Since

spectroscopic observations of the flare focused on the eastern edge of CR with weak intensities (Zhang & Ni 2018), precise Doppler velocities of the upflows could not be obtained. Anyway, the velocities of the upflows are in accordance with previous findings.

As to the driving mechanism of chromospheric evaporation, the roles of nonthermal electrons and thermal conduction have been largely investigated (e.g., Nagai & Emslie 1984; Abbett & Hawley 1999; Allred et al. 2005; Battaglia et al. 2009; Reep et al. 2015). During the C4.2 CRF as mentioned above, explosive chromospheric evaporation occurred on both CR and IR (Zhang et al. 2016a). Based on the quantitative calculation of electron energy flux and the spatial correspondence between the HXR source and IR, the authors concluded that the evaporation was driven by nonthermal electrons accelerated by magnetic reconnection. The estimated electron energy flux ($(1-4) \times 10^{10} \text{ erg cm}^{-2} \text{ s}^{-1}$) is sufficient to drive explosive evaporation as predicted by theory.

For the C5.5 flare in our study, direct HXR observations were unavailable during the impulsive phase. However, chromospheric evaporation occurs shortly after the coincident peak times in 1600 Å, 17 GHz, and SXR derivative, implying that the chromosphere responds very quickly to the impulsive energy deposition (Zhang et al. 2016b; Kumar et al. 2016; Hao et al. 2017; Song et al. 2018). Using one-dimensional hydrodynamic numerical simulations, Reep et al. (2015) investigated the importance of electron energy on the explosive and gentle evaporations and on the atmospheric response. It is found that for explosive evaporation, the atmospheric response does not depend strongly on electron energy, while for gentle evaporation, lower energy electrons are more efficient at heating the atmosphere and driving upflows. Comparing their results of maximal density, temperature, and velocity of the

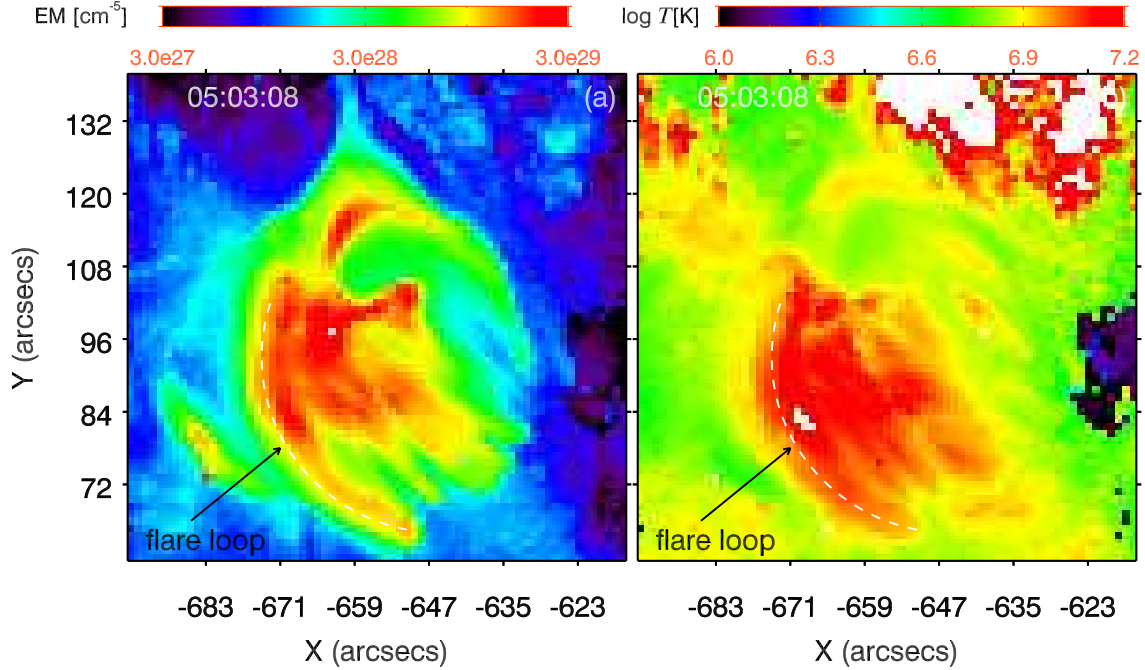


Figure 9. Emission measure map and temperature map of the flare at 05:03:08 UT. The black arrows point to the flare loop.

upflows across a broad range of electron energy (5–50 keV) and a broad range of energy flux (10^8 – 10^{11} erg cm $^{-2}$ s $^{-1}$), it is inferred that the electron energy flux above 5×10^{10} erg cm $^{-2}$ s $^{-1}$ are likely needed to explain our observations. It should be emphasized that the comparison between observations and simulations (even though this is beyond the scope of the present work) requires a proper forward modeling of different observables.

In addition to the total energy flux, the duration of heating is an important parameter that has effect on the atmospheric response. Reep et al. (2018) investigated the role of electron heating duration. It is found that the duration of upflows act as a good diagnostic of heating duration. In a multithreaded model, durations of 100–200 s can well reproduce both the red- and blueshifts for a fixed heating (see also Warren 2006). In Figure 1(b), the heating duration of ~ 240 s is labeled with an orange arrow, which is derived from the full width at half maximum (FWHM) of the HXR proxy. The heating duration is close to the results of nu-

merical simulations. In Figure 7(c), the time of converging motion from 04:58 UT to 05:04 UT is represented by a horizontal line. The decay time of upflow seems to be longer than the heating duration, which is probably due to the larger energy flux.

Reep & Russell (2016) developed a numerical model of flare heating due to the dissipation of Alfvénic waves propagating from the corona to the chromosphere. The waves damp themselves while propagating along the flux tubes as a result of collisions between electrons, ions, and neutrals, which decrease the wave amplitude and heat the local plasma. It is found that waves with sufficiently high frequencies and perpendicular wave numbers are able to heat the upper chromosphere and the corona. The temperatures of upper chromosphere and corona can rise up to $\sim 10^5$ K and a few MK within 10 s. Meanwhile, the heating can drive explosive evaporation, with the maximal blueshifted and redshifted velocities being ~ 200 km s $^{-1}$ and ~ 20 km s $^{-1}$. Hence, the atmospheric response to Alfvénic wave heating is similar to that of

heating by electron beam with a low-energy cut-off of 20 keV, a spectral index of 5, and an energy flux of 10^{10} erg cm⁻² s⁻¹ (see their Fig. 1). Without HXR imaging observations, it is impossible to distinguish the contributions of non-thermal electron and Alfvénic waves.

The energy flux of thermal conduction is expressed as

$$F_c \approx \kappa_0 T_e^{7/2} / L, \quad (5)$$

where $\kappa_0 \approx 10^{-6}$ erg K^{-2/7} cm⁻¹ s⁻¹ and L is the flare loop length (Wuelser et al. 1994). For the flare loop of CRF, F_c is estimated to be 5.5×10^8 erg cm⁻² s⁻¹, which is much lower than the requirement of electron beam energy flux. The timescale of thermal conduction is measured by the propagation time of thermal conduction front from the loop apex to the footpoints. The thermal conduction velocity is expressed as

$$v_0 = \frac{2\kappa_0 T_e^{5/2}}{3k_B n_e L_0}, \quad (6)$$

where k_B is the Boltzmann constant, L_0 represents the temperature scale height (Rust et al. 1985). Assuming that $L_0 = 6000$ km, v_0 is estimated to be ~ 1400 km s⁻¹. The timescale of thermal conduction is ~ 40 s. Therefore, thermal conduction as the main mechanism to heat the flare can be ruled out.

5. SUMMARY

In this work, we report our multiwavelength observations of the C5.5 CRF on 2014 August 24. The main results are summarized as follows:

1. The CRF was related to two coronal jets (jet1 and jet2) that propagated along large-scale closed loops. Jet1 appeared first with untwisting motion, while jet2 was generated 6 minutes later. The CRF consisted of a discrete CR with a diameter of $\sim 1'$ and a short IR inside. They were observed in UV, EUV, SXR, and especially in 17 GHz. The bright patches

in 17 GHz were cospatial with the flare ribbons. The CR and IR were associated with negative and positive polarities, implying a magnetic null point in the corona.

2. The peak times of the flare in 1600 Å, 17 GHz, and SXR derivative were coincident at $\sim 04:58$ UT, indicating the peak time of impulsive energy deposition in the lower atmosphere. Converging motion from the footpoints towards the loop top and filling process in the flare loops are revealed in AIA 131 Å and XRT filters (Be_{thin} and Be_{med}), which are clear evidence for chromospheric evaporation. The upflows started from $\sim 04:58$ UT until $\sim 05:04$ UT, covering the SXR peak time ($\sim 05:02$ UT). The temperature, density, and apparent velocities of upflows are $\sim 10^7$ K, 1.8×10^{10} cm⁻³, and 50–630 km s⁻¹ with a mean value of 170 km s⁻¹. The flare loops cooled down via thermal conduction with a timescale of 14 minutes and appeared progressively from 131 Å to 171 Å.
3. Despite of the lack of HXR observations, the requirement of electron energy flux is estimated to be above 5×10^{10} erg cm⁻² s⁻¹, while the energy flux of thermal conduction in heating the chromosphere is estimated to be 5.5×10^8 erg cm⁻² s⁻¹. Since heating by thermal conduction does not seem to provide enough energy, alternative mechanisms such as nonthermal electrons or Alfvénic waves might need to be invoked.

The authors appreciate the referee for valuable comments and suggestions to improve the quality of this article. We would also like to thank A. Warmuth and Z. J. Ning for fruitful discussions. *SDO* is a mission of NASA's Living With a Star Program. AIA and HMI data are courtesy of the NASA/*SDO*

science teams. This work is funded by NSFC (Nos. 11333009, 11790302, 11773079, 11603077, 11203083, U1731241, 11729301), the Fund of Jiangsu Province (BK20161618, BK20161095), and the Strategic Pioneer Program on Space

Science of CAS (XDA15052200 and XDA15320301). Q.M.Z is supported by the Youth Innovation Promotion Association CAS. D.L. is supported by the Specialized Research Fund for State Key Laboratories.

REFERENCES

- Acton, L. W., Leibacher, J. W., Canfield, R. C., et al. 1982, *ApJ*, 263, 409
- Abbett, W. P., & Hawley, S. L. 1999, *ApJ*, 521, 906
- Allred, J. C., Hawley, S. L., Abbett, W. P., & Carlsson, M. 2005, *ApJ*, 630, 573
- Aschwanden, M. J., Benz, A. O., Dennis, B. R., & Schwartz, R. A. 1995, *ApJ*, 455, 347
- Bastian, T. S., Benz, A. O., & Gary, D. E. 1998, *ARA&A*, 36, 131
- Battaglia, M., Fletcher, L., & Benz, A. O. 2009, *A&A*, 498, 891
- Brosius, J. W., & Phillips, K. J. H. 2004, *ApJ*, 613, 580
- Brosius, J. W., & Holman, G. D. 2010, *ApJ*, 720, 1472
- Brosius, J. W. 2013, *ApJ*, 762, 133
- Brown, J. C. 1971, *SoPh*, 18, 489
- Canfield, R. C., Metcalf, T. R., Zarro, D. M., & Lemen, J. R. 1990, *ApJ*, 348, 333
- Cargill, P. J. 1994, *ApJ*, 422, 381
- Carmichael, H. 1964, *NASA Special Publication*, 50, 451
- Czaykowska, A., De Pontieu, B., Alexander, D., & Rank, G. 1999, *ApJL*, 521, L75
- De Pontieu, B., Title, A. M., Lemen, J. R., et al. 2014, *SoPh*, 289, 2733
- Falchi, A., Qiu, J., & Cauzzi, G. 1997, *A&A*, 328, 371
- Fisher, G. H., Canfield, R. C., & McClymont, A. N. 1985, *ApJ*, 289, 414
- Fisher, G. H., Canfield, R. C., & McClymont, A. N. 1985, *ApJ*, 289, 425
- Fisher, G. H., Canfield, R. C., & McClymont, A. N. 1985, *ApJ*, 289, 434
- Fisher, G. H. 1989, *ApJ*, 346, 1019
- Fletcher, L., Dennis, B. R., Hudson, H. S., et al. 2011, *SSRv*, 159, 19
- Golub, L., Deluca, E., Austin, G., et al. 2007, *SoPh*, 243, 63
- Hao, Q., Yang, K., Cheng, X., et al. 2017, *Nature Communications*, 8, 2202
- Hirayama, T. 1974, *SoPh*, 34, 323
- Holman, G. D., Aschwanden, M. J., Aurass, H., et al. 2011, *SSRv*, 159, 107
- Jiang, C., Feng, X., Wu, S. T., & Hu, Q. 2013, *ApJL*, 771, L30
- Jing, J., Xu, Y., Cao, W., et al. 2016, *Scientific Reports*, 6, 24319
- Kopp, R. A., & Pneuman, G. W. 1976, *SoPh*, 50, 85
- Kosugi, T., Matsuzaki, K., Sakao, T., et al. 2007, *SoPh*, 243, 3
- Kumar, P., Nakariakov, V. M., & Cho, K.-S. 2016, *ApJ*, 822, 7
- Lemen, J. R., Title, A. M., Akin, D. J., et al. 2012, *SoPh*, 275, 17
- Li, D., Ning, Z. J., & Zhang, Q. M. 2015, *ApJ*, 813, 59
- Li, D., Ning, Z. J., Huang, Y., & Zhang, Q. M. 2017a, *ApJL*, 841, L9
- Li, H., Jiang, Y., Yang, J., et al. 2017b, *ApJ*, 836, 235
- Li, D., Li, Y., Su, W., Huang, Y., & Ning, Z. 2018, *ApJ*, 854, 26
- Liu, W., Liu, S., Jiang, Y. W., & Petrosian, V. 2006, *ApJ*, 649, 1124
- Masson, S., Pariat, E., Aulanier, G., & Schrijver, C. J. 2009, *ApJ*, 700, 559
- Milligan, R. O., Gallagher, P. T., Mathioudakis, M., & Keenan, F. P. 2006, *ApJL*, 642, L169
- Milligan, R. O., & Dennis, B. R. 2009, *ApJ*, 699, 968
- Milligan, R. O. 2015, *SoPh*, 290, 3399
- Nagai, F., & Emslie, A. G. 1984, *ApJ*, 279, 896
- Nakajima, H., Nishio, M., Enome, S., et al. 1994, *IEEE Proceedings*, 82, 705
- Neupert, W. M. 1968, *ApJL*, 153, L59
- Ning, Z., Cao, W., Huang, J., et al. 2009, *ApJ*, 699, 15
- Ning, Z., & Cao, W. 2010, *ApJ*, 717, 1232

- Nitta, S., Imada, S., & Yamamoto, T. T. 2012, *SoPh*, 276, 183
- Polito, V., Reeves, K. K., Del Zanna, G., Golub, L., & Mason, H. E. 2015, *ApJ*, 803, 84
- Polito, V., Reep, J. W., Reeves, K. K., et al. 2016, *ApJ*, 816, 89
- Reep, J. W., Bradshaw, S. J., & Alexander, D. 2015, *ApJ*, 808, 177
- Reep, J. W., & Russell, A. J. B. 2016, *ApJL*, 818, L20
- Reep, J. W., Polito, V., Warren, H. P., & Crump, N. A. 2018, *ApJ*, 856, 149
- Rubio da Costa, F., Liu, W., Petrosian, V., & Carlsson, M. 2015, *ApJ*, 813, 133
- Rust, D. M., Simnett, G. M., & Smith, D. F. 1985, *ApJ*, 288, 401
- Sadykov, V. M., Vargas Dominguez, S., Kosovichev, A. G., et al. 2015, *ApJ*, 805, 167
- Scherrer, P. H., Schou, J., Bush, R. I., et al. 2012, *SoPh*, 275, 207
- Shibata, K., & Magara, T. 2011, *Living Reviews in Solar Physics*, 8, 6
- Silva, A. V. R., Wang, H., Gary, D. E., Nitta, N., & Zirin, H. 1997, *ApJ*, 481, 978
- Song, Y. L., Guo, Y., Tian, H., et al. 2018, *ApJ*, 854, 64
- Sturrock, P. A. 1966, *Nature*, 211, 695
- Sun, X., Hoeksema, J. T., Liu, Y., Chen, Q., & Hayashi, K. 2012, *ApJ*, 757, 149
- Tian, H., Li, G., Reeves, K. K., et al. 2014, *ApJL*, 797, L14
- Tian, H., & Chen, N.-H. 2018, *ApJ*, 856, 34
- Wang, H., & Liu, C. 2012, *ApJ*, 760, 101
- Warmuth, A., & Mann, G. 2016a, *A&A*, 588, A115
- Warmuth, A., & Mann, G. 2016b, *A&A*, 588, A116
- Warren, H. P. 2006, *ApJ*, 637, 522
- Wueller, J.-P., Canfield, R. C., Acton, L. W., et al. 1994, *ApJ*, 424, 459
- Yang, S., Zhang, J., & Xiang, Y. 2015, *ApJL*, 798, L11
- Young, P. R., Doschek, G. A., Warren, H. P., & Hara, H. 2013, *ApJ*, 766, 127
- Young, P. R., Tian, H., & Jaeggli, S. 2015, *ApJ*, 799, 218
- Zhang, Q. M., Chen, P. F., Guo, Y., Fang, C., & Ding, M. D. 2012, *ApJ*, 746, 19
- Zhang, Q. M., & Ji, H. S. 2013, *A&A*, 557, L5
- Zhang, Q. M., & Ji, H. S. 2014, *A&A*, 567, A11
- Zhang, Q. M., Ning, Z. J., Guo, Y., et al. 2015, *ApJ*, 805, 4
- Zhang, Q. M., Li, D., Ning, Z. J., et al. 2016a, *ApJ*, 827, 27
- Zhang, Q. M., Li, D., & Ning, Z. J. 2016b, *ApJ*, 832, 65
- Zhang, Q. M., Ji, H. S., & Su, Y. N. 2016c, *SoPh*, 291, 859
- Zhang, Q. M., & Ni, L. 2018, 2018, arXiv:1811.08570